Numerical modelling of shock–bubble interactions using a pressure-based algorithm without Riemann solvers

Fabian Denner (✉), Berend G. M. van Wachem

Chair of Mechanical Process Engineering, Otto-von-Guericke-Universität Magdeburg, Universitätsplatz 2, 39106 Magdeburg, Germany

Abstract

The interaction of a shock wave with a bubble features in many engineering and emerging technological applications, and has been used widely to test new numerical methods for compressible interfacial flows. Recently, density-based algorithms with pressure-correction methods as well as fully-coupled pressure-based algorithms have been established as promising alternatives to classical density-based algorithms based on Riemann solvers. The current paper investigates the predictive accuracy of fully-coupled pressure-based algorithms without Riemann solvers in modelling the interaction of shock waves with one-dimensional and two-dimensional bubbles in gas–gas and liquid–gas flows. For a gas bubble suspended in another gas, the mesh resolution and the applied advection schemes are found to only have a minor influence on the bubble shape and position, as well as the behaviour of the dominant shock waves and rarefaction fans. For a gas bubble suspended in a liquid, however, the mesh resolution has a critical influence on the shape, the position and the post-shock evolution of the bubble, as well as the pressure and temperature distribution.

Research Article

1 Introduction

The interaction of a shock wave with a bubble is a process of broad academic and engineering interest, with applications in combustion and detonation (Michael and Nikiforakis, 2019), medical applications, e.g., shock-wave lithotripsy (Johnsen, 2007; Pan et al., 2018), in geophysics (Delale, 2013), and in microfluidics (Ando et al., 2012; Ohl and Ohl, 2016), featuring a rich variety of fluid dynamic and thermodynamic phenomena, such as compression and expansion waves, strong local heating, cavitation, evaporation and condensation, as well as the production of vorticity and turbulence (Ranjan et al., 2011; Delale, 2013). Shock–bubble interaction in a gas–gas flow is also used to study the interaction of shocks with gas inhomogeneities, whereas the shock-induced collapse of gas bubbles in liquids is of direct relevance to cavitating flows (Delale, 2013; Ohl and Ohl, 2016; Fuster, 2018). As a result, the fluid dynamics of shock–bubble interactions have been studied extensively, both experimentally (Haas and Sturtevant, 1987; Layes et al., 2003; Layes et al., 2005; Ranjan et al., 2007; Zhai et al., 2011) and computationally (Quirk and Karni, 1996; Bagabir and Drikakis, 2001; Johnsen, 2007; Niederhaus et al., 2008a, 2008b;

Johnsen and Colonius, 2009; Zhai et al., 2011; Hejazialhosseini et al., 2013; Xiang and Wang, 2017; Pan et al., 2018; Yoo and Sung, 2018; Michael and Nikiforakis, 2019). In addition, shock–bubble interactions have also been widely used as a canonical reference system to test and scrutinise new numerical schemes, see, e.g., Saurel and Abgrall (1999), Allaire et al. (2002), Hu and Khoo (2004), Nourgaliev et al. (2006), Chang and Liou (2007), Terashima and Tryggvason (2009), Kokh and Lagoutière (2010), Shukla et al. (2010), Shukla (2014), Wong and Lele (2017), and Denner et al. (2018).

Computational fluid dynamics has assumed an increasingly prominent role for the study and analysis of compressible interfacial flows, and especially for the study of shock–bubble interactions, over the past decades, as a result of rapidly advancing developments of the relevant numerical algorithms as well as the substantial computational resources routinely available nowadays. The numerical modelling of compressible interfacial flows thereby requires a consistent numerical treatment of the fluid interface that retains the main features of the solution, in particular the propagation of pressure waves (Abgrall and Saurel, 2003; Coralic and Colonius, 2014; Denner et al., 2018). However, the typically sharp change in Mach

✉ fabian.denner@ovgu.de

number at the fluid interface and the associated change in dominant physical mechanisms lead to distinct, and often contrasting, numerical requirements, which complicate the accurate and robust modelling of compressible fluid phenomena, such as the interaction of shock waves with gas bubbles. For instance, while the numerical algorithm has to ensure that the density is independent of the pressure and recovers a divergence-free velocity field in the incompressible limit (Chorin and Marsden, 1993; Hauke and Hughes, 1998), the accurate prediction of shock waves requires a conservative discretisation of the governing conservation laws (Hou and Floch, 1994).

Contemporary numerical methods for compressible interfacial flows are typically predicated on *density-based* algorithms, where the governing conservation equations are solved for the density, momentum, and total energy of the flow (Baer and Nunziato, 1986; Allaire et al., 2002; Murrone and Guillard, 2005; Coralic and Colonius, 2014). In these models, an exact or approximate Riemann solver is usually applied to evaluate the fluxes, with HLLC-type solvers (Toro et al., 1994) having gained particular popularity for interfacial flows (Shyue, 2006; Tokareva and Toro, 2010; Tian et al., 2011; Coralic and Colonius, 2014). The Ghost-Fluid method (GFM) (Fedkiw et al., 1999a) has established itself as a promising alternative to solving a Riemann problem (Fedkiw et al., 1999b; Terashima and Tryggvason, 2009; Bo and Grove, 2014), with recent extensions to improve the stability of simulations with strong shock–interface interactions and compressible gas–liquid flows (Liu et al., 2003; Wang et al., 2006; Liu and Hu, 2017). While density-based algorithms are naturally suited for compressible flows, they are poorly suited for low Mach number flows (Chorin, 1967; Karimian and Schneider, 1994; Wesseling, 2001; Cordier et al., 2012), where the coupling of pressure and density vanishes. Traditionally, tailored pre-conditioning techniques have been applied to extend density-based methods to low Mach number flows (Turkel et al., 1993; Turkel, 2006), which are however computationally very expensive for transient problems. This has been motivating recent work on combining density-based methods with segregated pressure-correction algorithms (Xiao, 2004; Moguen et al., 2012; Fuster and Popinet, 2018; Moguen et al., 2019) and *hybrid density/pressure-based* algorithms (van der Heul et al., 2003; Park and Munz, 2005), in which the continuity equation is solved for density but the energy equation is reformulated as an equation for pressure. An additional difficulty for interfacial flows associated with density-based methods is that the pressure field has to be reconstructed based on the applied thermodynamic closure model, which has proved to be a considerable difficulty in interfacial cells where two bulk phases coexist (Abgrall and Karni, 2001; Allaire et al.,

2002; Murrone and Guillard, 2005).

Pressure-based algorithms for compressible flows, in which the continuity equation is solved for pressure, are less prominent than their density-based counterparts. Deriving stable and efficient numerical schemes for the transonic regime, and formulating consistent shock-capturing schemes, are known to be difficult for pressure-based algorithms (Wesseling, 2001). However, because pressure plays an important role in all Mach number regimes, i.e., the pressure–velocity coupling dominates at low Mach numbers and the pressure–density coupling dominates at high Mach numbers (van Doormaal et al., 1987; Moukalled et al., 2016), pressure-based algorithms potentially offer a distinct advantage for applications in all Mach number regimes or in which the Mach number varies strongly, such as interfacial flows. Although, starting with the seminal work of Harlow and Amsden (1971a), a variety of pressure-based algorithms for compressible single-phase flows has been proposed, notably van Doormaal et al. (1987), Demirdžić et al. (1993), Karimian and Schneider (1994), and Xiao et al. (2017), it was only recently that Denner et al. (2018) proposed a conservative pressure-based algorithm for compressible interfacial flows at all speeds. This algorithm was proposed in conjunction with a new interface discretisation, the acoustically-conservative interface discretisation (ACID), that retains the acoustic features of the flow, which facilitates a rational definition of fluid properties in interfacial cells and which does not require Riemann solvers to compute the fluxes through the fluid interface. Denner et al. (2018) showed that such an algorithm yields unique definitions of the speed of sound and the Rankine–Hugoniot conditions in the interface region, and demonstrated a reliable prediction of acoustic and shock waves even in interfacial flows with acoustic impedance matching and shock impedance matching.

To model shock–bubble interactions, density-based algorithms in conjunction with Riemann-type solvers have been applied in most published studies to date (Quirk and Karni, 1996; Bagabir and Drikakis, 2001; Nourgaliev et al., 2006; Johnsen, 2007; Niederhaus et al., 2008b; Hejazialhosseini et al., 2013; Xiang and Wang, 2017). While exact Riemann solvers are prohibitively time consuming, approximate Riemann solvers require an *a priori* approximation of the characteristic wave speeds, which ensues a substantial complexity of the numerical algorithms (Saurel and Pantano, 2018). Thereby a strong dependence of the solution on the spatial resolution and the applied numerical schemes has been generally observed. For instance, a distinct feature of the shock–bubble interaction in gas–gas systems observed in numerical simulations of shock–bubble interactions, is instability (cf., Richtmyer–Meshkov instability (Brouillette,

2002)) forming on the interface as the shock wave passes. Noticeably, the shape and evolution of these interface instabilities depend strongly on the applied numerical methods (Johnsen and Colonius, 2006; Denner et al., 2018; Saurel and Pantano, 2018), e.g., the interface treatment or the advection schemes. In addition, these interface instabilities feature ever smaller lengthscales with an increasing spatial resolution of the simulation (Wong and Lele, 2017; Denner et al., 2018), although this is to be expected if surface tension, viscous stresses, and heat conduction are neglected, a common assumption, supported by experimental observations (Layes et al., 2003; Zhai et al., 2011), with reference to the small timescales considered in typical numerical simulations and the associated marginal influence of these effects, since there is no physical means to regulate or dissipate the small-scale flow features. However, the influences of the spatial resolution of the computational mesh and of the choice of discretisation schemes on the predictive quality of the modelling of shock–bubble interactions have not yet been studied comprehensively, especially in the context of pressure-based algorithms without Riemann solvers. It is, moreover, as yet unclear what influence such differences in interface instabilities have on the development and evolution of shock waves and rarefaction fans during and after the shock–bubble interaction, which is important for many of the associated engineering applications, especially in medical and bioengineering applications.

This article investigates the modelling of shock–bubble interactions using the pressure-based algorithm proposed by Denner et al. (2018), where the fluxes are evaluated with the ACID method and no Riemann solvers are applied. The aim is to identify the minimum spatial resolution requirements for a converged solution with respect to the primary flow quantities, as well as the influence of the discretisation scheme and of interface instabilities on the predictive accuracy of the main flow features, for shock–bubble interactions in both gas–gas and liquid–gas flows. As test-cases the shock interaction with a one-dimensional helium-bubble in air, a one-dimensional air-bubble in water, a two-dimensional R22-bubble in air, and a two-dimensional air-bubble in water are considered. While the shock–bubble interaction in gas–gas flows is not very sensitive to the employed discretisation schemes or the resolution of the computational mesh, the presented results demonstrate a very strong dependency of the primary flow quantities, especially temperature, on the spatial resolution of the computational mesh during the interaction of a shock wave with an air bubble suspended in water.

The governing equations are introduced in Section 2 and the numerical framework is presented in Section 3. The results of this study are presented and discussed in Section 4, and conclusions are drawn in Section 5.

2 Governing equations

The conservation laws governing fluid flow at all speeds, assuming viscous stresses and heat conduction are neglected, are the Euler equations, consisting of the conservation of mass:

$$\frac{\partial \rho}{\partial t} + \frac{\partial \rho u_i}{\partial x_i} = 0 \tag{1}$$

the conversation of momentum

$$\frac{\partial \rho u_j}{\partial t} + \frac{\partial \rho u_i u_j}{\partial x_i} = -\frac{\partial p}{\partial x_j} \tag{2}$$

and the conservation of energy

$$\frac{\partial \rho h}{\partial t} + \frac{\partial \rho u_i h}{\partial x_i} = \frac{\partial p}{\partial t} \tag{3}$$

where t is time, $\boldsymbol{u}$ is the velocity vector, p is pressure, ρ is the density, and $h = c_p T + u^2 / 2$ is the specific total enthalpy, with c_p the specific isobaric heat capacity and T the temperature. Gravity and surface tension are neglected in this study.

The stiffened-gas model (Harlow and Amsden, 1971b; Saurel et al., 2007) is applied to define the thermodynamic properties of the fluid and close the governing conservation laws. The density–pressure relationship is defined by the stiffened-gas equation of state (EOS):

$$\rho = \frac{p + \gamma_0 \Pi_0}{R_0 T} \tag{4}$$

where Π_0 is a fluid-dependent pressure constant, $R_0 = c_{p,0} - c_{v,0}$ is the specific heat capacity, and $\gamma_0 = c_{p,0} / c_{v,0}$ is the heat capacity ratio, with the reference specific isobaric heat capacity $c_{p,0}$ and the reference specific isochoric heat capacity $c_{v,0}$. The speed of sound is given as

$$a = \sqrt{\gamma_0 \frac{p + \Pi_0}{\rho}} = \sqrt{(\gamma_0 - 1) c_p T} \tag{5}$$

and the specific isobaric heat capacity is (Denner et al., 2018):

$$c_p = c_{p,0} \frac{p + \Pi_0}{p + \gamma_0 \Pi_0} \tag{6}$$

For $\Pi_0 = 0$, the stiffened-gas EOS reverts to the ideal-gas EOS, and the fluid is calorically perfect with $c_p = c_{p,0}$.

The Volume-of-Fluid (VOF) method (Hirt and Nichols, 1981) is adopted to capture the fluid interface between two immiscible bulk phases. To this end, the VOF method applies a colour function field ψ, defined as

$$\psi(\boldsymbol{x}) = \begin{cases} 0, & \boldsymbol{x} \in \Omega_{\text{a}} \\ 1, & \boldsymbol{x} \in \Omega_{\text{b}} \end{cases} \qquad (7)$$

where Ω_{a} and Ω_{b} are the subdomains occupied by fluids a and b, respectively, and $\Omega = \Omega_{\text{a}} \cup \Omega_{\text{b}}$ is the computational domain. The interface is located in every cell where $0 < \psi < 1$. Because the interface is a material front propagating with the flow (Denner et al., 2018), the colour function ψ is advected with the underlying fluid velocity by the advection equation:

$$\frac{\partial \psi}{\partial t} + u_i \frac{\partial \psi}{\partial x_i} = 0 \qquad (8)$$

3 Numerical framework

The numerical framework is based on the fully-coupled pressure-based algorithm of Denner et al. (2018), which is predicated on a finite-volume discretisation with collocated variable arrangement.

3.1 Temporal and spatial discretisation

The First-Order Backward Euler scheme (BDF1) and the Second-Order Backward Euler scheme (BDF2) are used to discretise the transient terms of the governing flow equations. The BDF1 scheme applied to the integrated transient term of a general flow variable ϕ is given for cell P as

$$\iiint_{V_P} \frac{\partial \phi}{\partial t} \bigg|_P \mathrm{d}V \approx \frac{\phi_P - \phi_P^{(t-\Delta t)}}{\Delta t} V_P \qquad (9)$$

and the BDF2 scheme is defined as

$$\iiint_{V_P} \frac{\partial \phi}{\partial t} \bigg|_P \mathrm{d}V \approx \frac{3\phi_P^{(t)} - 4\phi_P^{(t-\Delta t)} + \phi_P^{(t-2\Delta t)}}{2\Delta t} V_P \qquad (10)$$

where Δt is the time-step, superscript $(t - \Delta t)$ denotes values of the previous time-level, superscript $(t - 2\Delta t)$ denotes values of the previous-previous time-level, and V_P is the volume of mesh cell P. As previously suggested by Denner et al. (2018), for consistency all transient terms of the governing equations (1)–(3) are discretised with the same scheme.

Applying the divergence theorem, assuming the surface of the control volume has a finite number of flat faces f and applying the midpoint rule, the discretised advection terms of Eqs. (1)–(3) are given as

$$\iiint_{V_P} \frac{\partial \rho u_i \phi}{\partial x_i} \bigg|_P \mathrm{d}V \approx \sum_f \tilde{\rho}_f \vartheta_f \tilde{\phi}_f A_f \qquad (11)$$

where $\vartheta_f = \boldsymbol{u}_f \cdot \boldsymbol{n}_f$ is the advecting velocity of face f (see Section 3.2), $\boldsymbol{n}_f$ is the outward-pointing unit normal vector of face f, and A_f is the area of face f. The advected variable ϕ at face f is interpolated from the adjacent cell-centred values using a total variation diminishing (TVD) interpolation scheme (Denner and van Wachem, 2015), with which the face value is given as

$$\tilde{\phi}_f = \phi_U + \frac{\xi_f}{2}(\phi_D - \phi_U) \qquad (12)$$

where subscripts U and D denote the upwind and downwind cells respectively, and ξ_f is the flux limiter. In this study, the first-order upwind scheme ($\xi_f = 0$), the Minmod scheme, and the Superbee scheme (Roe, 1986) are considered.

3.2 Advecting velocity

The momentum-weighted interpolation (MWI) is applied to define an advecting velocity $\vartheta_f = \boldsymbol{u}_f \cdot \boldsymbol{n}_f$ at cell faces, which is used in the discretised advection terms of the governing equations. Following the unified formulation of the MWI proposed by Bartholomew et al. (2018), the advecting velocity ϑ_f at face f is given as

$$\vartheta_f = \overline{u}_{i,f} n_{i,f} - \hat{d}_f \left[\frac{\partial p}{\partial x_i}\bigg|_f - \frac{\rho_f^*}{2}\left(\frac{1}{\rho_P}\frac{\partial p}{\partial x_i}\bigg|_P + \frac{1}{\rho_Q}\frac{\partial p}{\partial x_i}\bigg|_Q\right)\right]n_{i,f}$$
$$+ \hat{d}_f \frac{\rho_f^{*(t-\Delta t_1)}}{\Delta t}\left(\vartheta_f^{(t-\Delta t)} - \overline{u}_{i,f}^{(t-\Delta t)} n_{i,f}\right) \qquad (13)$$

where subscript Q denotes the neighbour cell of P adjacent to face f, the interpolated face velocities $\overline{\boldsymbol{u}}_f$ and $\overline{\boldsymbol{u}}_f^{(t-\Delta t)}$ are obtained by linear interpolation, and the pressure gradient normal to face f is discretised as

$$\frac{\partial p}{\partial x_i}\bigg|_f n_{i,f} \approx \frac{p_Q - p_P}{\Delta x} \qquad (14)$$

The face density ρ_f^* is interpolated by a harmonic average (Bartholomew et al., 2018) and the coefficient $\hat{d}_f$ follows from the coefficients associated with the advection term (and shear stress term if viscosity is considered) of the momentum equations, as detailed in Bartholomew et al. (2018).

MWI provides a robust pressure–velocity coupling for incompressible and low Mach number flows by applying a low-pass filter acting on the third derivative of pressure (Bartholomew et al., 2018), thus avoiding pressure–velocity decoupling due to the collocated variable arrangement. As a result of the additional terms required to ensure a robust pressure–velocity coupling, the MWI introduces an unphysical dissipation of kinetic energy, which however diminishes with Δx^3 and is independent of Δt (Bartholomew et al.,

2018). The transient term of Eq. (13) ensures a time-step independent contribution of the MWI in conjunction with the coefficient $\hat{d}_f$ of the pressure term (Bartholomew et al., 2018) and including the transient term is important for a correct temporal evolution of pressure waves (Moguen et al., 2015; Bartholomew et al., 2018).

3.3 Discretised governing conservation laws

The discretised continuity equation (1) for cell P, applying the BDF1 scheme for clarity of presentation, is given as

$$\frac{\rho_P^{(n+1)} - \rho_P^{(t-\Delta t)}}{\Delta t} V_P + \sum_f \tilde{\rho}_f^{(n)} \vartheta_f^{(n+1)}$$
$$+ \tilde{\rho}_f^{(n+1)} \vartheta_f^{(n)} - \tilde{\rho}_f^{(n)} \vartheta_f^{(n)} A_f = 0 \qquad (15)$$

where the superscript (n) denotes known values of the most recent available solution and superscript $(n+1)$ denotes quantities which are solved implicitly. The advection term is linearized by a Newton linearization to facilitate a smooth transition from low to high Mach number regions (Karimian and Schneider, 1994; Kunz et al., 1999; Xiao et al., 2017). Following previous studies (Denner, 2018; Denner et al., 2018), the semi-implicit formulation of the advecting velocity is given as

$$\vartheta_f^{(n+1)} = \overline{u}_{i,f}^{(n+1)} n_{i,f} - \hat{d}_f \left[\frac{p_Q^{(n+1)} - p_P^{(n+1)}}{\Delta x} \right.$$
$$\left. - \frac{\rho_f^*}{2} \left(\frac{1}{\rho_P} \frac{\partial p}{\partial x_i} \bigg|_P^{(n)} + \frac{1}{\rho_Q} \frac{\partial p}{\partial x_i} \bigg|_Q^{(n)} \right) n_{i,f} \right]$$
$$+ \hat{d}_f \frac{\rho_f^{*(t-\Delta t)}}{\Delta t} \left(\vartheta_f^{(t-\Delta t)} - \overline{u}_{i,f}^{(t-\Delta t)} n_{i,f} \right) \qquad (16)$$

and the pressure-implicit formulation of the density is given as

$$\rho^{(n+1)} = \frac{p^{(n+1)} + \gamma_0 \Pi_0}{R_0 T} \qquad (17)$$

The discretised momentum equation (2) of cell P is given, with both the transient term and the advection term linearized by a Newton linearization (Denner, 2018; Denner et al., 2018) as

$$\frac{\rho_P^{(n)} u_{j,P}^{(n+1)} + \rho_P^{(n+1)} u_{j,P}^{(n)} - \rho_P^{(n)} u_{j,P}^{(n)} - \rho_P^{(t-\Delta t)} u_{j,P}^{(t-\Delta t)}}{\Delta t} V_P$$
$$+ \sum_f \left(\tilde{\rho}_f^{(n)} \vartheta_f^{(n)} \tilde{u}_{j,f}^{(n+1)} + \tilde{\rho}_f^{(n)} \vartheta_f^{(n+1)} \tilde{u}_{j,f}^{(n)} + \tilde{\rho}_f^{(n+1)} \vartheta_f^{(n)} \tilde{u}_{j,f}^{(n)} \right.$$
$$\left. - 2\tilde{\rho}_f^{(n)} \vartheta_f^{(n)} \tilde{u}_{j,f}^{(n)} \right) A_f$$
$$= - \sum_f \overline{p}_f^{(n+1)} n_{j,f} A_f \qquad (18)$$

with $\rho_P^{(n+1)}$ given by Eq. (17) and $\vartheta_f^{(n+1)}$ given by Eq. (16).

Similarly, the discretised energy equation (3) of cell P is given as

$$\frac{\rho_P^{(n)} h_P^{(n+1)} + \rho_P^{(n+1)} h_P^{(n)} - \rho_P^{(n)} h_P^{(n)} - \rho_P^{(t-\Delta t)} h_P^{(t-\Delta t)}}{\Delta t} V_P$$
$$+ \sum_f \left(\tilde{\rho}_f^{(n)} \vartheta_f^{(n)} \tilde{h}_f^{(n+1)} + \tilde{\rho}_f^{(n)} \vartheta_f^{(n+1)} \tilde{h}_f^{(n)} + \tilde{\rho}_f^{(n+1)} \vartheta_f^{(n)} \tilde{h}_f^{(n)} \right.$$
$$\left. - 2\tilde{\rho}_f^{(n)} \vartheta_f^{(n)} \tilde{h}_f^{(n)} \right) A_f$$
$$= \frac{p^{(n+1)} - p^{(t-\Delta t)}}{\Delta t} V_P \qquad (19)$$

3.4 Interface advection

The VOF advection equation (8) is discretised using a compressive VOF method (Denner and van Wachem, 2014; Denner et al., 2018). Following Denner et al. (2018), Eq. (8) is reformulated as

$$\frac{\partial \psi}{\partial t} + \frac{\partial u_i \psi}{\partial x_i} - \psi \frac{\partial u_i}{\partial x_i} = 0 \qquad (20)$$

Using the Crank–Nicolson scheme for the discretisation of the transient term, the semi-discretised form of Eq. (20) becomes

$$\frac{\psi_P - \psi_P^{(t-\Delta t_\psi)}}{\Delta t_\psi} V_P + \sum_f \frac{\psi_f + \psi_f^{(t-\Delta t_\psi)}}{2} \vartheta_f A_f$$
$$- \frac{\psi_P + \psi_P^{(t-\Delta t_\psi)}}{2} \sum_f \vartheta_f A_f = 0 \qquad (21)$$

where Δt_ψ is the time-step applied to advect the colour function ψ. The advection of the colour function is discretised using the same advecting velocity ϑ_f as for all advection terms of the governing equations. The face value ψ_f is interpolated using the CICSAM scheme (Ubbink and Issa, 1999), taking into account the orientation of the interface and the available flux volume. Excellent volume conservation has previously been demonstrated for this compressive VOF method for incompressible (Denner and van Wachem, 2014) and compressible flows (Denner et al., 2018).

3.5 Coupling of the bulk phases

The discretised governing equations presented in Section 3.3 are extended to interfacial flows using the acoustically-conservative interface discretisation (ACID) (Denner et al., 2018). The ACID method assumes that, for the purpose of discretising the governing conservation laws for a given cell, all cells in its finite-volume stencil are assigned the same colour function value, i.e., the colour function is assumed to be constant in the entire finite-volume stencil. The relevant thermodynamic properties that are discontinuous at the

interface, i.e., density and enthalpy, are evaluated based on the constant colour function field in the applied finite-volume stencil. This recovers the contact discontinuity associated with the interface (Anderson, 2003; Denner et al., 2018) and enables the application of the fully-conservative discretisation scheme presented in Section 3.3, identical to the one applied for single-phase flows.

3.5.1 Fluid properties

A hydrodynamic and thermodynamic consistent definition of the fluid properties for interfacial flows requires special consideration. The density of the fluid is defined based on the colour function ψ and the densities of the bulk phases as

$$\rho = (1 - \psi)\rho_a + \psi\rho_b \qquad (22)$$

where the partial densities ρ_a and ρ_b of the bulk phases are given by Eq. (4). This linear interpolation of the density is required for the discrete conservation of mass, momentum, and energy and is equivalent to an isobaric closure assumption for compressible interfacial flows (Allaire et al., 2002; Shyue, 2006). The heat capacity ratio also follows from the isobaric closure assumption as

$$\frac{1}{\gamma - 1} = \frac{1 - \psi}{\gamma_{0,a} - 1} + \frac{\psi}{\gamma_{0,b} - 1} \qquad (23)$$

The specific isobaric heat capacity is defined by a mass-weighted interpolation (Denner et al., 2018), which is essential for the conservation of the total energy, given as

$$c_p = \frac{(1 - \psi)\rho_a c_{p,a} + \psi\rho_b c_{p,b}}{\rho} \qquad (24)$$

where the partial densities ρ_a and ρ_b are given by Eq. (4), density ρ is given by Eq. (22), and the partial specific isobaric heat capacities $c_{p,a}$ and $c_{p,b}$ are given by Eq. (6). As shown by Denner et al. (2018), the speed of sound is defined throughout the domain based on Eq. (5) as $a = \sqrt{(\gamma - 1)c_p T}$, and the material-dependent pressure constant of the stiffened-gas model is given as $\Pi = [(\gamma - 1)\rho c_p T / \gamma] - p$, with the density ρ given by Eq. (22), the specific isobaric heat capacity c_p given by Eq. (24), and $(\gamma - 1)$ as well as γ given by Eq. (23).

3.5.2 Density treatment

Under the assumption that the colour function ψ is constant throughout the finite-volume stencil of cell P, the density interpolated to face f from the adjacent cell centre is given as

$$\tilde{\rho}_f = \rho_U^\star + \frac{\xi_f}{2}(\rho_D^\star - \rho_U^\star) \qquad (25)$$

The density ρ_U at the upwind cell U and ρ_D at the downwind cell D are given based on the colour function value of cell P by Eq. (22), so that

$$\rho_U^\star = \rho_{a,U} + \psi_P(\rho_{b,U} - \rho_{a,U}) \qquad (26)$$

and

$$\rho_D^\star = \rho_{a,D} + \psi_P(\rho_{b,D} - \rho_{a,D}) \qquad (27)$$

The density at previous time-levels is evaluated in a similar fashion based on the colour function value of cell P, with (Denner et al., 2018):

$$\rho_P^{(t-\Delta t)} = \rho_{a,P}^{(t-\Delta t)} + \psi_P\left(\rho_{b,P}^{(t-\Delta t)} - \rho_{a,P}^{(t-\Delta t)}\right) \qquad (28)$$

and likewise for $\rho_P^{(t-2\Delta t)}$, if required.

3.5.3 Enthalpy treatment

The specific total enthalpy at face f is given, again assuming the colour function ψ is constant throughout the finite-volume stencil of cell P, as (Denner et al., 2018):

$$\tilde{h}_f = \frac{1}{\tilde{\rho}_f}\left[\rho_U^\star h_U^\star + \frac{\xi_f}{2}\left(\rho_D^\star h_D^\star - \rho_U^\star h_U^\star\right)\right] \qquad (29)$$

with $\tilde{\rho}_f$ given by Eq. (25), where the specific total enthalpy of the upwind and downwind cells are given as

$$h_U^\star = c_{p,U}^\star T_U + \frac{1}{2}\boldsymbol{u}_U^2 \qquad (30)$$

$$h_D^\star = c_{p,D}^\star T_D + \frac{1}{2}\boldsymbol{u}_D^2 \qquad (31)$$

respectively, $\rho_U^\star$ is given by Eq. (26), and $\rho_D^\star$ is given by Eq. (27). The specific isobaric heat capacities $c_{p,U}^\star$ and $c_{p,D}^\star$ are defined by Eq. (24) with ψ_P as

$$c_{p,U}^\star = \frac{\rho_{a,U}c_{p,a,U} + \psi_P(\rho_{b,U}c_{p,b,U} - \rho_{a,U}c_{p,a,U})}{\rho_U^\star} \qquad (32)$$

and

$$c_{p,D}^\star = \frac{\rho_{a,D}c_{p,a,D} + \psi_P(\rho_{b,D}c_{p,b,D} - \rho_{a,D}c_{p,a,D})}{\rho_D^\star} \qquad (33)$$

Since the specific total enthalpy is a primary solution variable, a deferred correction approach as proposed by Denner et al. (2018) is applied to enforce Eq. (29).

The specific total enthalpy at the previous time-levels follow analogously as (Denner et al., 2018):

$$h_P^{(t-\Delta t)} = c_{p,P}^{\star,(t-\Delta t)} T_P^{(t-\Delta t)} + \frac{1}{2}\boldsymbol{u}_P^{(t-\Delta t),2} \qquad (34)$$

with

$$c_{p,P}^{\star,(t-\Delta t)} = \frac{\rho_{a,P}^{(t-\Delta t)} c_{p,a,P}^{(t-\Delta t)} + \psi_P \left(\rho_{b,P}^{(t-\Delta t)} c_{p,b,P}^{(t-\Delta t)} - \rho_{a,P}^{(t-\Delta t)} c_{p,a,P}^{(t-\Delta t)} \right)}{\rho_P^{(t-\Delta t)}}$$

(35)

and likewise for $h_P^{(t-2\Delta t)}$ and $c_{p,P}^{\star,(t-2\Delta t)}$, if required.

3.6 Solution procedure

The discretised governing equations presented in Section 3.3 are solved simultaneously in a single linear system of equations (Denner, 2018; Denner et al., 2018), $A\chi = b$, where A is the coefficient matrix of size $5N \times 5N$, $\chi \equiv (u, p, h)^{\mathrm{T}}$ is the solution vector of length $5N$ of the primary solution variables, b is the right-hand side vector containing all known contributions, and N is the number of mesh cells of the three-dimensional computational mesh. The solution procedure performs nonlinear iterations in which the linear system of governing equations is solved using the *Block–Jacobi* preconditioner and the *BiCGSTAB* solver of the software library PETSc (Balay et al., 2017), as described in detail by Denner (2018).

4 Results

The presented results focus on the spatial resolution requirements and discretisation necessary for the accurate prediction of shock–bubble interactions using a pressure-based algorithm. As already comprehensively demonstrated by Denner et al. (2018), the applied numerical algorithm captures shock waves and rarefaction fans accurately in single-phase flows and interfacial flows, with a robust convergence under mesh refinement and a precise prediction of the Rankine–Hugoniot relations also in interfacial cells.

4.1 One-dimensional helium-bubble in air

The interaction of a shock wave travelling in air with Mach number $M_s = 1.1$ and interacting with a helium bubble in a one-dimensional domain with a length of 1 m is considered. The initial post-shock conditions (I) are

$$u_{\mathrm{I}} = 55.33 \text{ m/s}, \quad p_{\mathrm{I}} = 1.245 \times 10^5 \text{ Pa}, \quad T_{\mathrm{I}} = 319.48 \text{ K}$$

and the pre-shock conditions (II) are

$$u_{\mathrm{II}} = 0 \text{ m/s}, \quad p_{\mathrm{II}} = 10^5 \text{ Pa}, \quad T_{\mathrm{II}} = 300 \text{ K}$$

Air is taken to have a heat capacity ratio of $\gamma_{0,\mathrm{Air}} = 1.4$ and a specific gas constant of $R_{0,\mathrm{Air}} = 288.0 \text{ J} \cdot \text{kg}^{-1} \cdot \text{K}^{-1}$, and helium is assumed to have a heat capacity ratio of $\gamma_{0,\mathrm{He}} = 1.648$ and a specific gas constant of $R_{0,\mathrm{He}} = 1581.2 \text{ J} \cdot \text{kg}^{-1} \cdot \text{K}^{-1}$. The shock is initially located at $x_0 = 0.3$ m, the helium bubble occupies the interval $0.5 \leq x \leq 0.7$, and the applied time-step corresponds to a Courant number of $Co = a_{\mathrm{II},\mathrm{He}} \Delta t / \Delta x = 0.44$.

The results, shown in Fig. 1, are obtained on equidistant meshes with three mesh resolutions resolving the one-dimensional domain with 200, 1000, and 5000 cells, which corresponds to a spatial resolution of 40, 200, and 1000 cells for the initial length of the helium bubble, respectively. The distribution of pressure, velocity, and temperature within the one-dimensional domain depends considerably on the applied mesh resolution. While this may be a problem for the accurate local prediction of pressure, velocity, and temperature, as well as the related thermodynamic or chemical processes, the position of the primary shock wave as it travels through the bubble is, apart from the sharpness of the discontinuity, unaffected by the mesh resolution. In addition, the colour function ψ and the density ρ (both not shown) are in very good agreement on the different meshes. All quantities obtained with the finest mesh resolution, 1000 cells for the initial length of the helium bubble, are in excellent agreement with the corresponding exact Riemann solution.

4.2 One-dimensional air-bubble in water

The interaction of a shock wave travelling in water with Mach number $M_s = 1.1$ and interacting with an air bubble in a one-dimensional domain with a length of 2 m is considered. The initial post-shock conditions (I) are

$$u_{\mathrm{I}} = 100.45 \text{ m/s}, \quad p_{\mathrm{I}} = 1.487 \times 10^8 \text{ Pa}, \quad T_{\mathrm{I}} = 302.61 \text{ K}$$

and the pre-shock conditions (II) are

(a) Velocity u (b) Pressure $\Delta p = p - p_{\mathrm{II}}$ (c) Temperature T
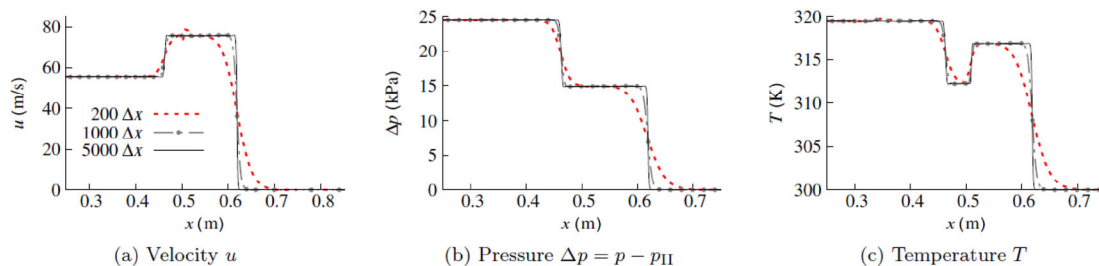
Fig. 1 Profiles of the velocity u, pressure $\Delta p = p - p_{\mathrm{II}}$, and temperature T of the interaction of a shock wave with $M_s = 1.1$ with a one-dimensional helium-bubble in air on meshes with different mesh spacings Δx at time $t = 6.5 \times 10^{-4}$ s.

$$u_{II} = 0 \text{ m/s}, \quad p_{II} = 10^5 \text{ Pa}, \quad T_{II} = 300 \text{ K}$$

Water is taken to have a heat capacity ratio of $\gamma_{0,\text{Water}} = 4.1$, a pressure constant of $\Pi_{0,\text{Water}} = 4.4 \times 10^8 \text{ Pa}$, and a specific gas constant of $R_{0,\text{Water}} = 6000 \text{ J} \cdot \text{kg}^{-1} \cdot \text{K}^{-1}$, and air is taken to have a heat capacity ratio of $\gamma_{0,\text{Air}} = 1.4$, a pressure constant of $\Pi_{0,\text{Air}} = 0 \text{ Pa}$, and a specific gas constant of $R_{0,\text{Air}} = 288.0 \text{ J} \cdot \text{kg}^{-1} \cdot \text{K}^{-1}$. The shock is initially located at $x_0 = 1.1 \text{ m}$, the air bubble occupies the interval $1.3 \leq x \leq 1.5$, and the applied time-step corresponds to $Co = a_{II,\text{Water}} \Delta t / \Delta x = 0.45$.

The results are obtained on equidistant meshes with three mesh resolutions, resolving the one-dimensional domain with 400, 2000, and 10,000 cells, which corresponds to a spatial resolution of 40, 200, and 1000 cells for the initial length of the air bubble, respectively, as considered in the previous section for the helium bubble in air. As observed in Fig. 2, the density is principally in good agreement on all three meshes, whereas the temperature distribution inside the bubble appears to be especially sensitive to the mesh resolution, with visible differences between the results obtained on the coarsest mesh compared to the results obtained on the two meshes with higher resolution. Furthermore, the pressure upstream of the water–air interface after the shock wave has passed exhibits a considerable dependency on the mesh resolution, as seen in Fig. 3. The pressure is significantly underpredicted compared to the exact Riemann solution at both time-instances shown in Fig. 3, with an underprediction of approximately 1.5×10^5 Pa on the coarsest mesh and

approximately 0.6×10^5 Pa on the finest mesh. Despite these differences in pressure and temperature, the position of the primary shock wave as it travels through the bubble is, apart from the sharpness of the discontinuity, still in very good agreement on the meshes corresponding to 200 and 1000 cells for the initial length of the air bubble. On the coarsest considered mesh, corresponding to 40 cells for the initial length of the air bubble, however, the position of the shock wave has an offset in the downstream direction, which may be attributed to an overprediction of the speed of sound as the shock wave passes the interface.

4.3 Two-dimensional R22-bubble in air

The interaction of a shock wave with $M_s = 1.22$ in air with a circular R22 bubble is simulated, a shock–bubble interaction which has previously been studied experimentally (Haas and Sturtevant, 1987) and numerically (Quirk et al., 2008b). The computational setup is schematically illustrated in Fig. 4. The shock wave is initially situated at $x = 0.17 \text{ m}$ and travels from left to right at speed u_s. The shock wave separates the post-shock region (I) and the pre-shock region (II), which are initialized with

$$u_I = 125.65 \text{ m/s}, \quad p_I = 1.59060 \times 10^5 \text{ Pa}, \quad T_I = 402.67 \text{ K}$$

$$u_{II} = 0 \text{ m/s}, \quad p_{II} = 1.01325 \times 10^5 \text{ Pa}, \quad T_{II} = 351.82 \text{ K}$$

Air is taken to have a heat capacity ratio of $\gamma_{0,\text{Air}} = 1.4$ and a specific gas constant of $R_{0,\text{Air}} = 288.0 \text{ J} \cdot \text{kg}^{-1} \cdot \text{K}^{-1}$, and R22
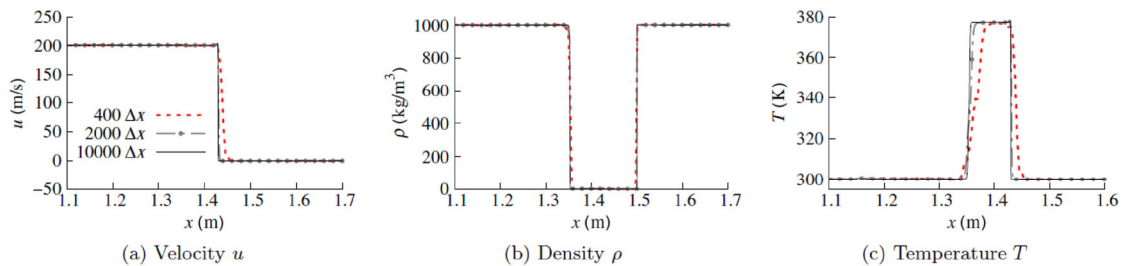

Fig. 2   Profiles of the velocity u, density ρ, and temperature T of the interaction of a shock wave with $M_s = 1.1$ with a one-dimensional air-bubble in water on meshes with different mesh spacings Δx at time $t = 4.0 \times 10^{-4} \text{ s}$.
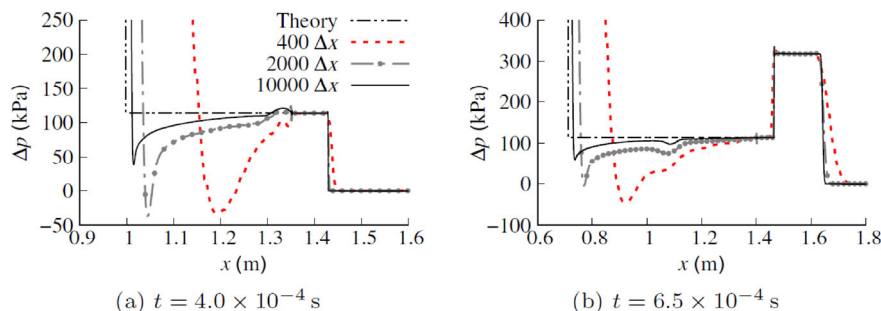

Fig. 3   Profiles of the pressure $\Delta p = p - p_{II}$ of the interaction of a shock wave with $M_s = 1.1$ with a one-dimensional air-bubble in water on meshes with different mesh spacings Δx at time (a) $t = 4.0 \times 10^{-4} \text{ s}$ and (b) $t = 6.5 \times 10^{-4} \text{ s}$. The theoretical Riemann solution is shown as a reference.
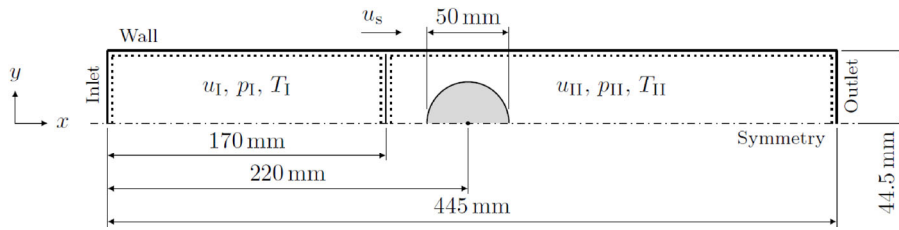
Fig. 4 Schematic illustration of the computational setup of the two-dimensional R22 bubble in air interacting with a shock wave with Mach number $M_s = 1.22$. The shock wave is initially located at $x = 0.17$ m and travels from left to right. The shaded area represents the bubble with a diameter of $d_0 = 0.05$ m, with the bubble centre initially located at $x = 0.22$ m.

is assumed to have a heat capacity ratio of $\gamma_{0,R22} = 1.249$ and a specific gas constant of $R_{0,R22} = 90.885 \text{ J} \cdot \text{kg}^{-1} \cdot \text{K}^{-1}$. The applied computational mesh is equidistant and Cartesian, and the applied time-step corresponds to a Courant number of $Co = a_{II,Air} \Delta t / \Delta x = 0.38$.

Figures 5 and 6 show the contours of the density gradient and the pressure distribution at different dimensionless time $\tau = t a_{II,R22} / d_0$ for equidistant Cartesian meshes with mesh resolutions of 200, 300, and 500 cells per initial bubble diameter d_0. While the overall shape as well as the position of the bubble predicted on the different meshes are largely the same, interface instabilities with smaller structures

develop as the mesh resolution increases. As mentioned in the introduction, this is to be expected, yet a coherent and sufficiently accurate description of the magnitude and frequency with which these instabilities occur in reality is presently not available. These interface instabilities generate acoustic waves, as seen in Figs. 5 and 6, which however do not affect the position, shape, and strength of the dominant flow structures, i.e., shock waves and rarefaction fans. In general it is noticeable in Figs. 5 and 6, that the overall impact of the mesh resolution on the observed flow features is minor, apart from the interface instabilities developing as a result of the passing shock wave and the resolution of
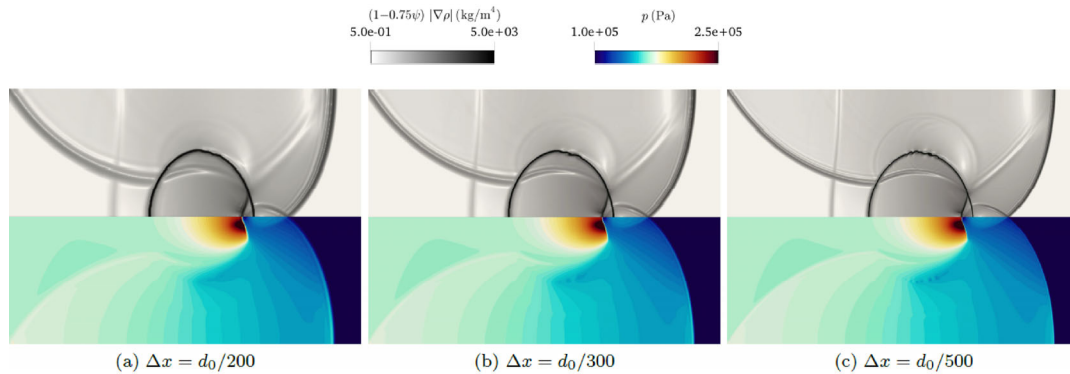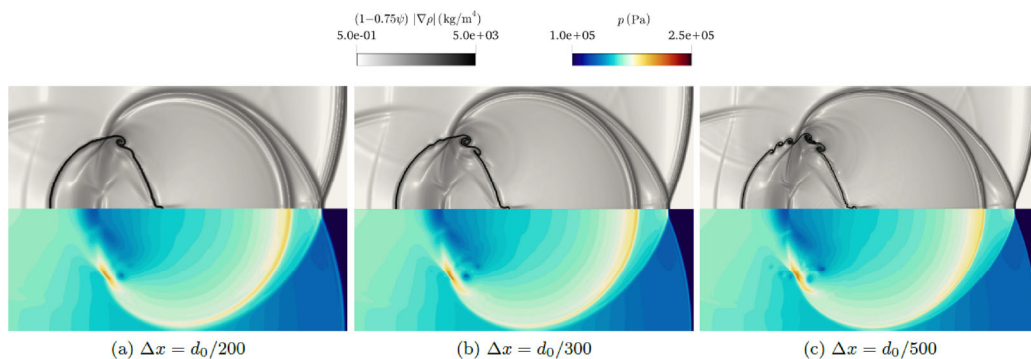

Fig. 5 Contours of the density gradient $(1 - 0.75\psi) | \nabla \rho |$ (upper half) and the pressure p (lower half) of the two-dimensional shock–bubble interaction of the R22 bubble in air on a Cartesian mesh with different mesh resolutions Δx at $\tau = t a_{II,R22} / d_0 = 0.68$, using the Minmod scheme.

Fig. 6 Contours of the density gradient $(1 - 0.75\psi) | \nabla \rho |$ (upper half) and the pressure p (lower half) of the two-dimensional shock–bubble interaction of the R22 bubble in air on a Cartesian mesh with different mesh resolutions Δx at $\tau = t a_{II,R22} / d_0 = 1.15$, using the Minmod scheme.

the shock waves and rarefaction fans. This observation is supported by the density profiles along the x-axis (direction of travel of the primary shock wave) shown in Fig. 7, which exhibit very little differences for the three considered mesh resolutions.

Considering different TVD differencing schemes for the discretisation of advected variables (see Section 3.1) lead to very similar observations as mesh refinement, applying a more compressive differencing scheme facilitates and increases the generation of interface instabilities. Figure 8 shows the contours of the density gradient and the pressure distribution at dimensionless time $\tau = 1.15$ on a mesh with a mesh resolution of 500 cells per initial bubble diameter d_0, using (in order of increasing compression) the first-order upwind

scheme, the Minmod scheme, and the Superbee scheme. The interface advection is unaffected by this choice and identical for all these cases, discretised as described in Section 3.4. Applying different TVD advection schemes only influences the development of interface instabilities, while the position and overall shape of the R22 bubble are largely the same. The strong instabilities observed at the interface when the Superbee scheme is applied, and the ensuing acoustic waves, can be clearly observed in Fig. 8, yet it is also apparent that the different resolution of the discontinuities and the interface instabilities developing with the Minmod and Superbee schemes have very little influence on the position and strength of the dominant shock waves and rarefaction fans. The density profiles along the x-axis in Fig. 9 support this
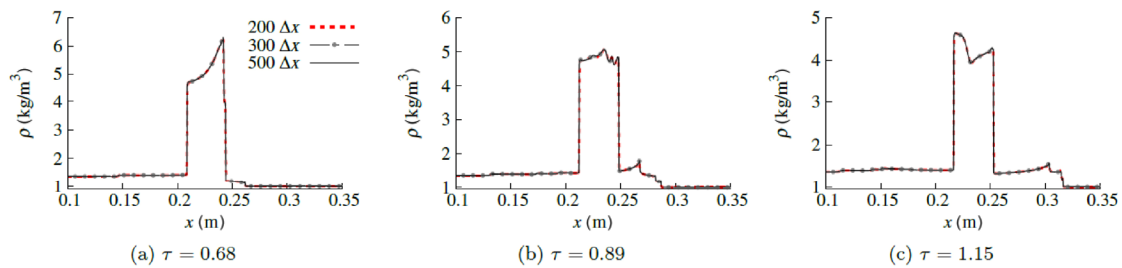

Fig. 7 Profiles of the density ρ along the x-axis at $y = 0.005$ m of the two-dimensional shock–bubble interaction of the R22 bubble in air on Cartesian meshes with different mesh spacings Δx at different dimensionless time $\tau = t\, a_{\mathrm{II,R22}} / d_0$, using the Minmod scheme.

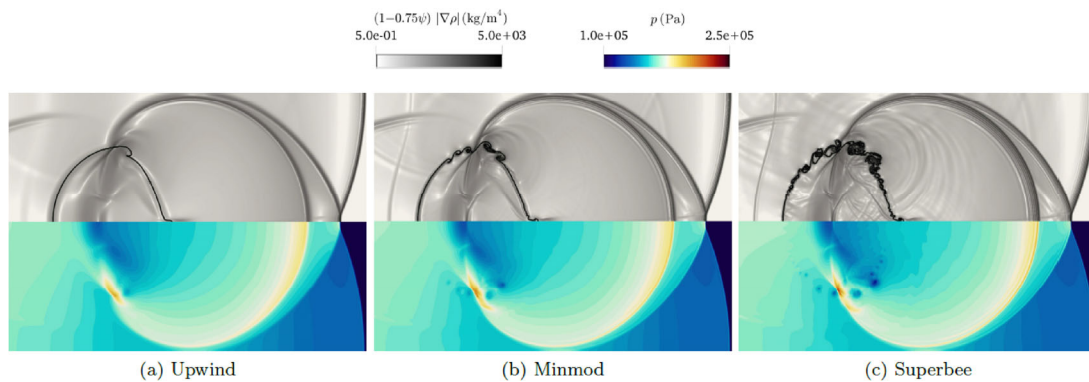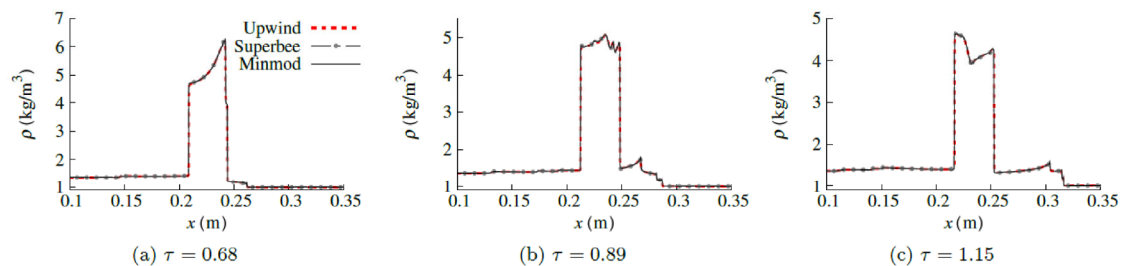**Fig. 8** Contours of the density gradient $(1 - 0.75\psi)\,|\nabla\rho|$ (upper half) and the pressure p (lower half) of the two-dimensional shock–bubble interaction of the R22 bubble in air on a Cartesian mesh with $\Delta x = d_0 / 500$ at $\tau = t\, a_{\mathrm{II,R22}} / d_0 = 1.15$, using the first-order upwind scheme, the Minmod scheme, and Superbee scheme.

Fig. 9 Profiles of the density ρ along the x-axis at $y = 0.005$ m of the two-dimensional shock–bubble interaction of the R22 bubble in air on Cartesian meshes with mesh spacing $\Delta x = d_0 / 500$ at different dimensionless time $\tau = t\, a_{\mathrm{II,R22}} / d_0$, using the first-order upwind scheme, the Minmod scheme, and the Superbee scheme.

observation.

4.4   Two-dimensional air-bubble in water

The interaction of a shock wave with $M_s = 1.72$ in water with a circular air bubble is simulated, as considered previously in other studies (Nourgaliev et al., 2006; Shukla, 2014; Haimovich and Frankel, 2017; Goncalves et al., 2019). The computational setup is schematically illustrated in Fig. 10. The shock is initially situated at $x = 6.6 \times 10^{-3}$ m and travels from left to right at speed u_s. The shock wave separates the post-shock region (I) and the pre-shock region (II), which are initialised with

$$u_I = 685.25 \text{ m/s}, \quad p_I = 1.91530 \times 10^5 \text{ Pa}, \quad T_I = 381.80 \text{ K}$$

$$u_{II} = 0 \text{ m/s}, \quad p_{II} = 10^5 \text{ Pa}, \quad T_{II} = 293.15 \text{ K}$$

Water is taken to have a heat capacity ratio of $\gamma_{0,\text{Water}} = 4.1$, a pressure constant of $\Pi_{0,\text{Water}} = 4.4 \times 10^8$ Pa, and a specific gas constant of $R_{0,\text{Water}} = 6000$ J·kg^{-1}·K^{-1}, and air is taken to have a heat capacity ratio of $\gamma_{0,\text{Air}} = 1.4$, a pressure
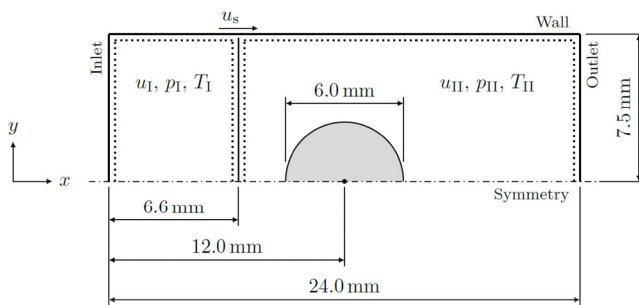

Fig. 10 Schematic illustration of the computational setup of the air bubble in water interacting with a shock wave with Mach number $M_s = 1.72$. The shock wave is initially located at $x_{s,0} = 6.6 \times 10^{-3}$ m and travels from left to right. The shaded area represents the air bubble with a diameter of $d_0 = 6.0 \times 10^{-3}$ m, with the bubble centre initially located at $x_{b,0} = 12.0 \times 10^{-3}$ m.

constant of $\Pi_{0,\text{Air}} = 0$ Pa, and a specific gas constant of $R_{0,\text{Air}} = 288.0$ J·kg^{-1}·K^{-1}. The applied computational mesh is equidistant and Cartesian, and the applied time-step corresponds to a Courant number of $Co = a_{II,\text{Water}}\Delta t / \Delta x = 0.11$.

Figures 11–13 show the contours of the pressure and temperature distribution of the water–air system at different time t for equidistant Cartesian meshes with a mesh resolution of 200, 400, and 600 cells per initial bubble diameter d_0. Contrary to the rather similar solutions obtained on different meshes for the gas–gas shock–bubble interaction in Section 4.3, the evolution of the shock–bubble interaction of the air bubble in water is strongly dependent on the mesh resolution. In particular the temperature distribution inside the air bubble exhibits distinct differences on the considered meshes, with generally higher temperatures predicted when the mesh resolution is increased. These differences are especially pronounced when the primary shock wave travels through the bubble, e.g., at $t = 3.0$ μs, where the higher temperature appears to influence the position of the shock wave considerably, as seen in Fig. 14(c). Despite these differences in temperature distribution and position of the shock wave at $t = 3.0$ μs, which are much less pronounced in the pressure and density fields shown in Fig. 14, the results obtained on the meshes with 400 and 600 cells per initial bubble diameter d_0 are in reasonably good agreement at the later stages of the shock–bubble interaction, as seen in Figs. 15 and 16. In fact, similar observations with respect to the mesh dependency for the same shock–bubble interaction were recently reported by Shukla (2014) and Goncalves et al. (2019) using density-based methods. The mesh with 200 cells per initial bubble diameter d_0, on the other hand, yields significantly different results compared to the meshes with higher resolution, which affects the position of the shock wave as well as the shape of the bubble, as evident by comparing Fig. 11(c) with
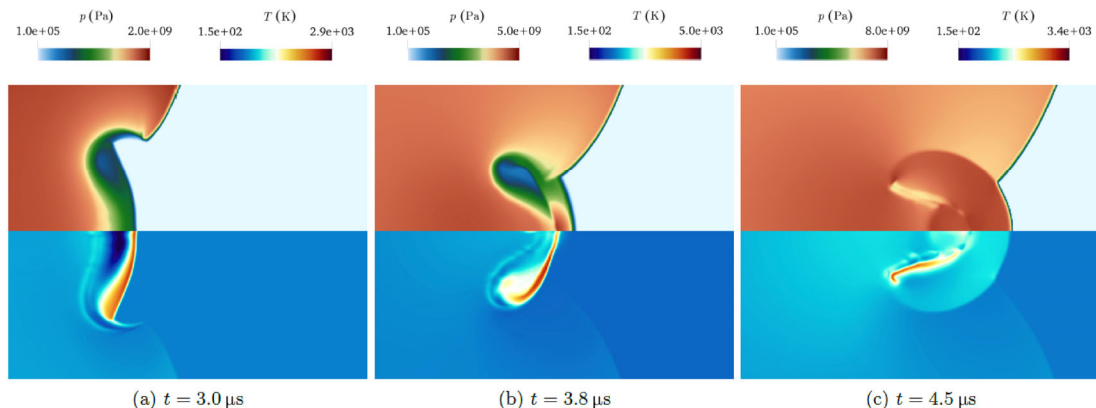

(a) $t = 3.0$ μs   (b) $t = 3.8$ μs   (c) $t = 4.5$ μs

Fig. 11 Contours of the pressure p (upper half) and the temperature T (lower half) of the two-dimensional shock–bubble interaction of the air bubble in water on a Cartesian mesh with $\Delta x = d_0 / 200$ at different time t. Both the pressure scale and the temperature scale are logarithmic.
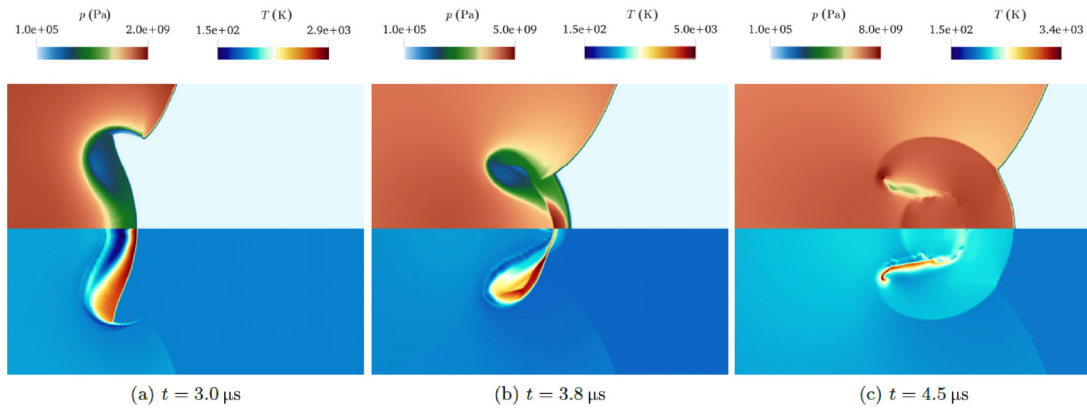
(a) $t = 3.0\,\mu s$ (b) $t = 3.8\,\mu s$ (c) $t = 4.5\,\mu s$

Fig. 12 Contours of the pressure p (upper half) and the temperature T (lower half) of the two-dimensional shock–bubble interaction of the air bubble in water on a Cartesian mesh with $\Delta x = d_0\,/\,400$ at different time t. Both the pressure scale and the temperature scale are logarithmic.

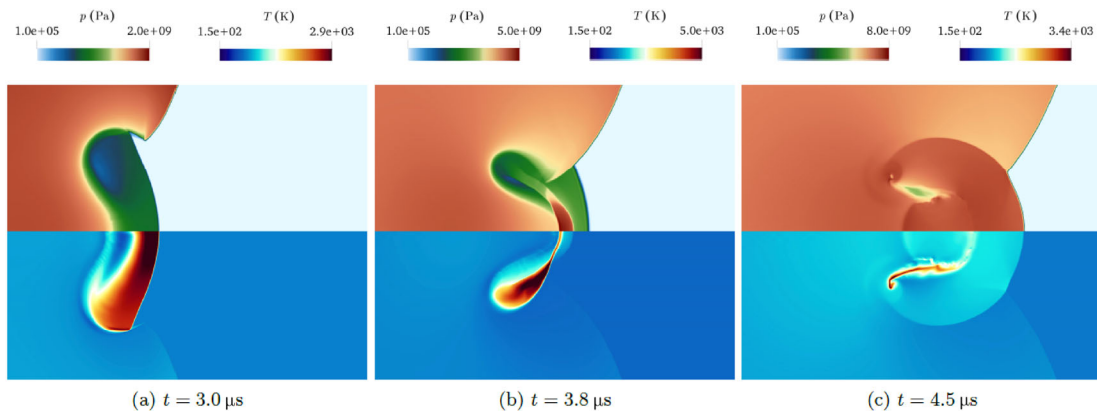(a) $t = 3.0\,\mu s$ (b) $t = 3.8\,\mu s$ (c) $t = 4.5\,\mu s$

Fig. 13 Contours of the pressure p (upper half) and the temperature T (lower half) of the two-dimensional shock–bubble interaction of the air bubble in water on a Cartesian mesh with $\Delta x = d_0\,/\,600$ at different time t. Both the pressure scale and the temperature scale are logarithmic.
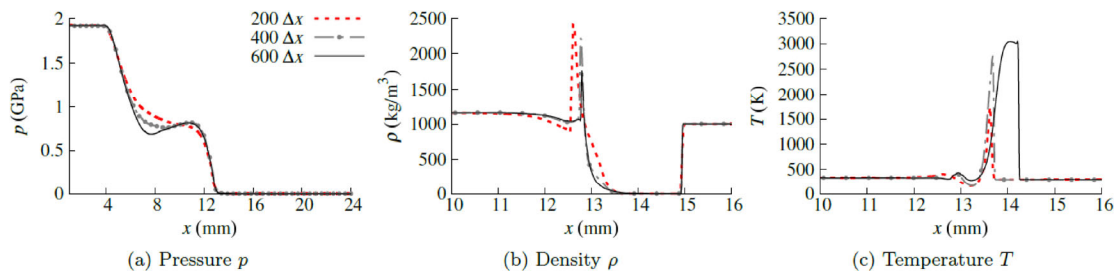

(a) Pressure p (b) Density ρ (c) Temperature T

Fig. 14 Profiles of pressure p, density ρ, and temperature T along the x-axis at $y = 6 \times 10^{-4}$ m of the two-dimensional shock–bubble interaction of the air bubble in water on Cartesian meshes with different mesh spacings Δx at time $t = 3.0 \times 10^{-6}$ s.

(a) Pressure p (b) Density ρ (c) Temperature T

Fig. 15 Profiles of pressure p, density ρ, and temperature T along the x-axis at $y = 6 \times 10^{-4}$ m of the two-dimensional shock–bubble interaction of the air bubble in water on Cartesian meshes with different mesh spacings Δx at time $t = 3.8 \times 10^{-6}$ s.
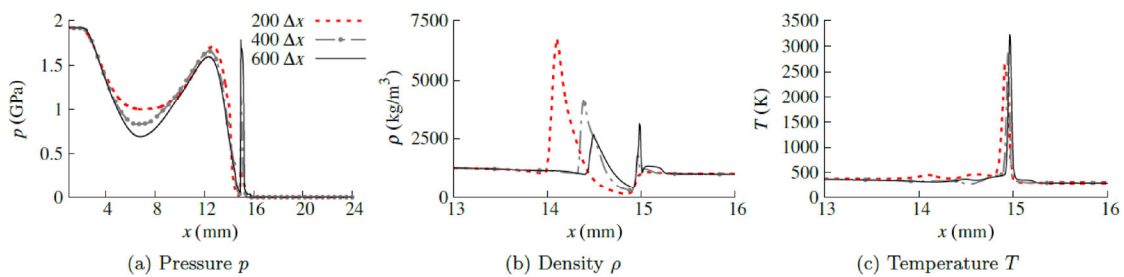
Fig. 16 Profiles of pressure p, density ρ, and temperature T along the x-axis at $y = 6 \times 10^{-4}$ m of the two-dimensional shock–bubble interaction of the air bubble in water on Cartesian meshes with different mesh spacings Δx at time $t = 4.5 \times 10^{-6}$ s.
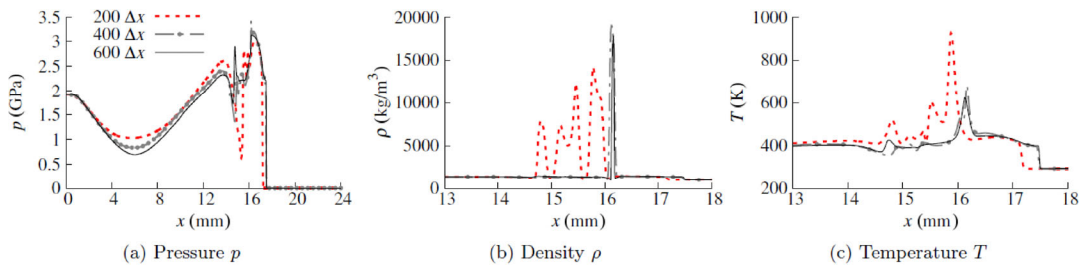
Fig. 12(c), and by the density profiles in Figs. 14(b), 15(b), and 16(b).

5 Conclusions

In the current paper, the numerical modelling of shock–bubble interactions using the pressure-based algorithm proposed by Denner et al. (2018), where the fluxes are evaluated with the ACID method and no Riemann solvers are applied, has been investigated. While shock–bubble interactions in gas–gas flows are largely of academic interest, the interaction of shock waves with a bubble suspended in a liquid is encountered in many different engineering and emerging technological applications, especially in microfluidics and medical applications. Of course, an accurate prediction of shock–bubble interactions is, therefore, a prerequisite for numerical methods to be utilized in research and process development pertaining to these applications.

The presented results have demonstrated a very strong dependency of the interaction of a shock wave with an air bubble suspended in water on the spatial resolution of the computational mesh. In particular, the temperature field has been found to exhibit large differences between different mesh resolutions, which also contribute to differences in the propagation of the primary shock wave. To this end, for the shock interaction with the air bubble in water, the presented results suggest a mesh resolution of at least 400–600 cells per initial diameter to yield reasonably converged results. However, even though the position of the shock wave as well as the pressure, temperature, and density fields have been found to yield agreement for such a mesh resolution at later stages of the shock–bubble interaction, i.e., after the shock wave has passed the bubble, these quantities still exhibit considerable differences while the shock wave passes through the bubble. Considering the rapid and significant increase in pressure, temperature, and density as the bubble is compressed when the shock wave passes, the accuracy of the ideal-gas model also warrants further study, since the evolution of the bubble collapse has been shown by the presented results to be strongly dependent on the quality and accuracy of the prediction of pressure and temperature.

Shock–bubble interactions also provide a convenient canonical reference system to test and scrutinize new numerical schemes for the simulation of compressible interfacial flows; shock–bubble interaction can be found in most publications that propose a new numerical scheme for compressible interfacial flows. These tests mostly focus on gas–gas flows, e.g., the R22 bubble in air also considered in this study, while the computationally more expensive and challenging shock–bubble interaction in liquid–gas flows is frequently neglected. However, the presented results show that the shock–bubble interaction in a gas–gas flow is not sensitive to the employed numerical methods and the spatial resolution of the computational mesh, contrary to the shock–bubble interaction in a liquid–gas flow. This puts the informative value of validating numerical schemes using gas–gas shock–bubble interactions into question and strongly suggests that the shock–bubble interaction in liquid–gas flows is generally better suited to scrutinize and compare numerical methods for compressible interfacial flows.

References

Abgrall, R., Karni, S. 2001. Computations of compressible multifluids. *J Comput Phys*, 169: 594–623.

Abgrall, R., Saurel, R. 2003. Discrete equations for physical and numerical compressible multiphase mixtures. *J Comput Phys*, 186: 361–396.

Allaire, G., Clerc, S., Kokh, S. 2002. A five-equation model for the simulation of interfaces between compressible fluids. *J Comput Phys*, 181: 577–616.

Anderson, J. D. 2003. *Modern Compressible Flow: With a Historical Perspective*. McGraw-Hill New York.

Ando, K., Liu, A.-Q., Ohl, C.-D. 2012. Homogeneous nucleation in water in microuidic channels. *Phys Rev Lett*, 109: 044501.

Baer, M. R., Nunziato, J. W. 1986. A two-phase mixture theory for the deflagration-to-detonation transition (ddt) in reactive granular materials. *Int J Multiphase Flow*, 12: 861–889.

Bagabir, A., Drikakis, D. 2001. Mach number effects on shock–bubble interaction. *Shock Waves*, 11: 209–218.

Balay, S., Abhyankar, S., Adams, M. F., Brown, J., Brune, P., Buschelman, K., Dalcin, L. D., Eijkhout, V., Gropp, W., Kaushik, D., Knepley, M., May, D., McInnes, L. C., Munson, T., Rupp, K., Sanan, P.,

Smith, B., Zampini, S., Zhang, H., Zhang, H. 2017. PETSc users manual revision 3.8. Technical Report. ANL-95/11 - Revision 3.8. Argonne National Laboratory.

Bartholomew, P., Denner, F., Abdol-Azis, M. H., Marquis, A., van Wachem, B. G. M. 2018. Unified formulation of the momentum-weighted interpolation for collocated variable arrangements. *J Comput Phys*, 375: 177–208.

Bo, W., Grove, J. W. 2014. A volume of fluid method based ghost fluid method for compressible multi-fluid flows. *Comput Fluid*, 90: 113–122.

Brouillette, M. 2002. The Richtmyer–Meshkov instability. *Ann Rev Fluid Mech*, 34: 445–468.

Chang, C.-H., Liou, M.-S. 2007. A robust and accurate approach to computing compressible multiphase flow: Stratified flow model and AUSM+-up scheme. *J Comput Phys*, 225: 840–873.

Chorin, A. J. 1967. A numerical method for solving incompressible viscous flow problems. *J Comput Phys*, 2: 12–26.

Chorin, A. J., Marsden, J. E. 1993. *A Mathematical Introduction to Fluid Mechanics*. Springer Verlag.

Coralic, V., Colonius, T. 2014. Finite-volume WENO scheme for viscous compressible multicomponent flows. *J Comput Phys*, 274: 95–121.

Cordier, F., Degond, P., Kumbaro, A. 2012. An asymptotic-preserving all-speed scheme for the Euler and Navier–Stokes equations. *J Comput Phys*, 231: 5685–5704.

Delale, C. F. 2013. *Bubble Dynamics and Shock Waves*. Springer Berlin Heidelberg.

Demirdžić, I., Lilek, Ž., Perić, M. 1993. A collocated finite volume method for predicting flows at all speeds. *Int J Numer Meth Fluids*, 16: 1029–1050.

Denner, F. 2018. Fully-coupled pressure-based algorithm for compressible flows: Linearisation and iterative solution strategies. *Comput Fluid*, 175: 53–65.

Denner, F., van Wachem, B. 2015. TVD differencing on three-dimensional unstructured meshes with monotonicity-preserving correction of mesh skewness. *J Comput Phys*, 298: 466–479.

Denner, F., van Wachem, B. G. M. 2014. Compressive VOF method with skewness correction to capture sharp interfaces on arbitrary meshes. *J Comput Phys*, 279: 127–144.

Denner, F., Xiao, C.-N., van Wachem, B. G. M. 2018. Pressure-based algorithm for compressible interfacial flows with acoustically-conservative interface discretisation. *J Comput Phys*, 367: 192–234.

Fedkiw, R. P., Aslam, T., Merriman, B., Osher, S. 1999a. A non-oscillatory eulerian approach to interfaces in multimaterial flows (the ghost fluid method). *J Comput Phys*, 152: 457–492.

Fedkiw, R. P., Aslam, T., Xu, S. J. 1999b. The ghost fluid method for deflagration and detonation discontinuities. *J Comput Phys*, 154: 393–427.

Fuster, D. 2018. A review of models for bubble clusters in cavitating flows. *Flow Turbulence Combust*, 102: 497–536.

Fuster, D., Popinet, S. 2018. An all-Mach method for the simulation of bubble dynamics problems in the presence of surface tension. *J Comput Phys*, 374: 752–768

Goncalves, E., Hoarau, Y., Zeidan, D. 2019. Simulation of shock-induced bubble collapse using a four-equation model. *Shock Waves*, 29: 221–234.

Haas, J.-F., Sturtevant, B. 1987. Interaction of weak shock waves with cylindrical and spherical gas inhomogeneities. *J Fluid Mech*, 181: 41.

Haimovich, O., Frankel, S. H. 2017. Numerical simulations of compressible multicomponent and multiphase flow using a high-order targeted ENO (TENO) finite-volume method. *Comput Fluid*, 146: 105–116.

Harlow, F. H., Amsden, A. A. 1971a. A numerical fluid dynamics calculation method for all flow speeds. *J Comput Phys*, 8: 197–213.

Harlow, F., Amsden, A. 1971b. Fluid Dynamics, Monograph LA-4700. Los Alamos National Laboratory.

Hauke, G., Hughes, T. J. R. 1998. A comparative study of different sets of variables for solving compressible and incompressible flows. *Comput Method Appl M*, 153: 1–44.

Hejazialhosseini, B., Rossinelli, D., Koumoutsakos, P. 2013. Vortex dynamics in 3D shock–bubble interaction. *Phys Fluid*, 25: 110816.

Hirt, C. W., Nichols, B. D. 1981. Volume of fluid (VOF) method for the dynamics of free boundaries. *J Comput Phys*, 39: 201–225.

Hou, T. Y., Floch, P. G. L. 1994. Why nonconservative schemes converge to wrong solutions: Error analysis. *Math Comput*, 62: 497–530.

Hu, X. Y., Khoo, B. C. 2004. An interface interaction method for compressible multifluids. *J Comput Phys*, 198: 35–64.

Johnsen, E. 2007. Numerical simulations of non-spherical bubble collapse: With applications to shockwave lithotripsy. Ph.D. Thesis. California Institute of Technology, USA.

Johnsen, E. R. I. C., Colonius, T. I. M. 2009. Numerical simulations of non-spherical bubble collapse. *J Fluid Mech*, 629: 231–262.

Johnsen, E., Colonius, T. 2006. Implementation of WENO schemes in compressible multicomponent flow problems. *J Comput Phys*, 219: 715–732.

Karimian, S. M. H., Schneider, G. E. 1994. Pressure-based computational method for compressible and incompressible flows. *J Thermophys Heat Tr*, 8: 267–274.

Kokh, S., Lagoutière, F. 2010. An anti-diffusive numerical scheme for the simulation of interfaces between compressible fluids by means of a five-equation model. *J Comput Phys*, 229: 2773–2809.

Kunz, R. F., Cope, W. K., Venkateswaran, S. 1999. Development of an implicit method for multi-fluid flow simulations. *J Comput Phys*, 152: 78–101.

Layes, G., Jourdan, G., Houas, L. 2003. Distortion of a spherical gaseous interface accelerated by a plane shock wave. *Phys Rev Lett*, 91: 174502.

Layes, G., Jourdan, G., Houas, L. 2005. Experimental investigation of the shock wave interaction with a spherical gas inhomogeneity. *Phys Fluid*, 17: 028103.

Liu, C., Hu, C. H. 2017. Adaptive THINC-GFM for compressible multi-medium flows. *J Comput Phys*, 342: 43–65.

Liu, T. G., Khoo, B. C., Yeo, K. S. 2003. Ghost fluid method for strong shock impacting on material interface. *J Comput Phys*, 190: 651–681.

Michael, L., Nikiforakis, N. 2019. The evolution of the temperature field during cavity collapse in liquid nitromethane. Part I: Inert case. *Shock Waves*, 29: 153–172.

Moguen, Y., Bruel, P., Dick, E. 2015. Solving low Mach number Riemann problems by a momentum interpolation method. *J Comput Phys*, 298: 741–746.

Moguen, Y., Bruel, P., Dick, E. 2019. A combined momentum-interpolation and advection upstream splitting pressure-correction algorithm for simulation of convective and acoustic transport at all levels of Mach number. *J Comput Phys*, 384: 16–41.

Moguen, Y., Kousksou, T., Bruel, P., Vierendeels, J., Dick, E. 2012. Pressure–velocity coupling allowing acoustic calculation in low Mach number flow. *J Comput Phys*, 231: 5522–5541.

Moukalled, F., Mangani, L., Darwish, M. 2016. *The Finite Volume Method in Computational Fluid Dynamics: An Advanced Introduction with OpenFOAM and Matlab*. Springer.

Murrone, A., Guillard, H. 2005. A five equation reduced model for compressible two phase flow problems. *J Comput Phys*, 202: 664–698.

Niederhaus, J. H. J., Greenough, J. A., Oakley, J. G., Bonazza, R. 2008a. Vorticity evolution in two- and three-dimensional simulations for shock–bubble interactions. *Phys Scripta*, T132: 014019.

Niederhaus, J. H. J., Greenough, J. A., Oakley, J. G., Ranjan, D., Anderson, M. H., Bonazza, R. 2008b. A computational parameter study for the three-dimensional shock–bubble interaction. *J Fluid Mech*, 594: 85–124.

Nourgaliev, R. R., Dinh, T. N., Theofanous, T. G. 2006. Adaptive characteristics-based matching for compressible multifluid dynamics. *J Comput Phys*, 213: 500–529.

Ohl, S.-W., Ohl, C.-D. 2016. Acoustic cavitation in a microchannel. In: *Handbook of Ultrasonics and Sonochemistry*. Springer Singapore, 99–135.

Pan, S., Adami, S., Hu, X., Adams, N. A. 2018. Phenomenology of bubble-collapse-driven penetration of biomaterial-surrogate liquid–liquid interfaces. *Phys Rev Fluids*, 3: 114005.

Park, J. H., Munz, C.-D. 2005. Multiple pressure variables methods for fluid flow at all Mach numbers. *Int J Numer Meth Fluids*, 49: 905–931.

Quirk, J. J., Karni, S. 1996. On the dynamics of a shock–bubble interaction. *J Fluid Mech*, 318: 129.

Ranjan, D., Niederhaus, J., Motl, B., Anderson, M., Oakley, J., Bonazza, R. 2007. Experimental investigation of primary and secondary features in high-Mach-number shock-bubble interaction. *Phys Rev Lett*, 98: 024502.

Ranjan, D., Oakley, J., Bonazza, R. 2011. Shock–bubble interactions. *Annu Rev Fluid Mech*, 43: 117–140.

Roe, P. 1986. Characteristic-based schemes for the Euler equations. *Ann Rev Fluid Mech*, 18: 337–365.

Saurel, R., Abgrall, R. 1999. A simple method for compressible multifluid flows. *SIAM J Sci Comput*, 21: 1115–1145.

Saurel, R., Le Métayer, O., Massoni, J., Gavrilyuk, S. 2007. Shock jump relations for multiphase mixtures with stiff mechanical relaxation. *Shock Waves*, 16: 209–232.

Saurel, R., Pantano, C. 2018. Diffuse-interface capturing methods for compressible two-phase flows. *Ann Rev Fluid Mech*, 50: 105–130.

Shukla, R. K. 2014. Nonlinear preconditioning for efficient and accurate interface capturing in simulation of multicomponent compressible flows. *J Comput Phys*, 276: 508–540.

Shukla, R. K., Pantano, C., Freund, J. B. 2010. An interface capturing method for the simulation of multi-phase compressible flows. *J Comput Phys*, 229: 7411–7439.

Shyue, K.-M. 2006. A volume-fraction based algorithm for hybrid barotropic and non-barotropic two-fluid flow problems. *Shock Waves*, 15: 407–423.

Terashima, H., Tryggvason, G. 2009. A front-tracking/ghost-fluid method for fluid interfaces in compressible flows. *J Comput Phys*, 228: 4012–4037.

Tian, B. L., Toro, E. F., Castro, C. E. 2011. A path-conservative method for a five-equation model of two-phase flow with an HLLC-type Riemann solver. *Comput Fluid*, 46: 122–132.

Tokareva, S. A., Toro, E. F. 2010. HLLC-type Riemann solver for the Baer–Nunziato equations of compressible two-phase flow. *J Comput Phys*, 229: 3573–3604.

Toro, E. F., Spruce, M., Speares, W. 1994. Restoration of the contact surface in the HLL-Riemann solver. *Shock Waves*, 4: 25–34.

Turkel, E. 2006. Numerical methods and nature. *J Sci Comput*, 28: 549–570.

Turkel, E., Fiterman, A., van Leer, B. 1993. Preconditioning and the limit to the incompressible flow equations. Technical Report. NASA CR-191500. Institute for Computer Applications in Science and Engineering Hampton VA, USA.

Ubbink, O., Issa, R. I. 1999. A method for capturing sharp fluid interfaces on arbitrary meshes. *J Comput Phys*, 153: 26–50.

Van der Heul, D. R., Vuik, C., Wesseling, P. 2003. A conservative pressure-correction method for flow at all speeds. *Comput Fluid*, 32: 1113–1132.

Van Doormaal, J. P., Raithby, G. D., McDonald, B. H. 1987. The segregated approach to predicting viscous compressible fluid flows. *J Turbomach*, 109: 268–277.

Wang, C. W., Liu, T. G., Khoo, B. C. 2006. A real ghost fluid method for the simulation of multimedium compressible flow. *SIAM J Sci Comput*, 28: 278–302.

Wesseling, P. 2001. *Principles of Computational Fluid Dynamics*. Springer.

Wong, M. L., Lele, S. K. 2017. High-order localized dissipation weighted compact nonlinear scheme for shock- and interface-capturing in compressible flows. *J Comput Phys*, 339: 179–209.

Xiang, G., Wang, B. 2017. Numerical study of a planar shock interacting with a cylindrical water column embedded with an air cavity. *J Fluid Mech*, 825: 825–852.

Xiao, C.-N., Denner, F., van Wachem, B. G. M. 2017. Fully-coupled pressure-based finite-volume framework for the simulation of fluid flows at all speeds in complex geometries. *J Comput Phys*, 346: 91–130.

Xiao, F. 2004. Unified formulation for compressible and incompressible flows by using multi-integrated moments I: One-dimensional inviscid compressible flow. *J Comput Phys*, 195: 629–654.

Yoo, Y.-L., Sung, H.-G. 2018. Numerical investigation of an interaction between shock waves and bubble in a compressible multiphase flow using a diffuse interface method. *Int J Heat Mass Tran*, 127: 210–221.

Zhai, Z., Si, T., Luo, X., Yang, J. 2011. On the evolution of spherical gas interfaces accelerated by a planar shock wave. *Phys Fluid*, 23: 084104.